The ALMA Survey of 70 μm Dark High-mass Clumps in Early Stages (ASHES). XII. Unanchored Forked Stream in the Propagating Path of a

The Astrophysical Journal, 990:229 (17pp), 2025 September 10 https://doi.org/10.3847/1538-4357/adf208

The ALMA Survey of 70 μm Dark High-mass Clumps in Early Stages (ASHES). XII. Unanchored Forked Stream in the Propagating Path of a Protostellar Outflow

Shuting Lin[1], Siyi Feng (冯思轶)[1], Patricio Sanhueza[2], Ke Wang (王科)[3,4], Zhi-Yu Zhang (张智昱)[5,6], Yichen Zhang[7], Fengwei Xu[3,4], Junzhi Wang[8], Kaho Morii[9,10,11], Hauyu Baobab Liu[12,13], Sheng-Yuan Liu[14], Lile Wang[3,4], Hui Li[15], Daniel Tafoya[16], Willem Baan[17,18], Shanghuo Li[5,6], and Giovanni Sabatini[19]
[1] Department of Astronomy, Xiamen University, Zengcuo'an West Road, Xiamen, 361005; syfeng@xmu.edu.cn
[2] Department of Astronomy, School of Science, The University of Tokyo, 7-3-1 Hongo, Bunkyo, Tokyo 113-0033, Japan
[3] Kavli Institute for Astronomy and Astrophysics, Peking University, 5 Yiheyuan Road, Haidian District, Beijing 100871
[4] Department of Astronomy, School of Physics, Peking University, Beijing 100871
[5] School of Astronomy and Space Science, Nanjing University, Nanjing 210093
[6] Key Laboratory of Modern Astronomy and Astrophysics (Nanjing University), Ministry of Education, Nanjing 210093
[7] Department of Astronomy, Shanghai Jiao Tong University, 800 Dongchuan Road, Minhang, Shanghai 200240
[8] School of Physical Science and Technology, Guangxi University, Nanning 530004
[9] Center for Astrophysics | Harvard & Smithsonian, 60 Garden Street, Cambridge, MA 02138, USA
[10] Department of Astronomy, Graduate School of Science, The University of Tokyo, 7-3-1 Hongo, Bunkyo-ku, Tokyo 113-0033, Japan
[11] National Astronomical Observatory of Japan, National Institutes of Natural Sciences, 2-21-1 Osawa, Mitaka, Tokyo 181-8588, Japan
[12] Department of Physics, National Sun Yat-Sen University, No. 70, Lien-Hai Road, Kaohsiung City 80424
[13] Center of Astronomy and Gravitation, National Taiwan Normal University, Taipei 116
[14] Institute of Astronomy and Astrophysics, Academia Sinica, 11F of Astronomy-Mathematics Building, AS/NTU No. 1, Section 4, Roosevelt Road
[15] Department of Astronomy, Tsinghua University, Haidian DS 100084, Beijing
[16] Department of Space, Earth and Environment, Chalmers University of Technology, Onsala Space Observatory, SE-43992 Onsala, Sweden
[17] Xinjiang Astronomical Observatory, CAS, 150 Science 1-Street, Urumqi, Xinjiang 830011
[18] Netherlands Institute for Radio Astronomy ASTRON, NL-7991 PD Dwingeloo, The Netherlands
[19] INAF, Osservatorio Astrofisico di Arcetri, Largo E. Fermi 5, I-50125, Firenze, Italy
Received 2025 April 24; revised 2025 July 4; accepted 2025 July 18; published 2025 September 10

Abstract

Outflows are key indicators of ongoing star formation. We report the discovery of an unanchored forked stream within the propagating path of an extremely young protostellar outflow in the 70 μm-dark clump G34.74-0.12, based on Atacama Large Millimeter/submillimeter Array (ALMA) 1.3 mm observations with an angular resolution of 1.″6 (~5000 au). This outflow originates from a 9.7 $M_\odot$ core, exhibits a fork-shaped stream structure in its redshifted lobe, which is traced by CO (2–1), SiO (5–4), and H_2CO ($3_{0,3}$–$2_{0,2}$). It has a momentum of 13 $M_\odot$ km s^{-1}, an energy of 107 $M_\odot$ km^2 s^{-2}, and a dynamical timescale of $\sim 10^4$ yr. Significantly, the enhanced relative abundances of SiO, H_2CO, and CH_3OH with respect to CO, along with the increased temperature at the forked point, indicate a collisional origin. The forked point does not coincide with any dust continuum core >0.1 $M_\odot$. Moreover, CO (2–1) emission also traces three other outflows in this region, characterized by their masses (0.40, 0.02, and 0.15 $M_\odot$) and momenta (5.2, 0.2, and 1.8 $M_\odot$ km s^{-1}), as part of the ALMA Survey of 70 μm dark High-mass clumps in Early Stages project. All the newly discovered morphological and kinematic features associated with these extremely young protostellar outflows (with timescales of 10^3–10^4 yr) suggest that the initial stages of star formation are more complicated than previously understood.

Unified Astronomy Thesaurus concepts: Infrared dark clouds (787); Star forming regions (1565); Star formation (1569); Interstellar medium (847); Interstellar line emission (844)

1. Introduction

Infrared dark clouds (IRDCs) exhibit high extinction, appearing as dark features against the bright Galactic infrared background, and are considered the most likely birthplaces of high-mass and low-mass stars (e.g., J. M. Rathborne et al. 2006; M. M. Dunham et al. 2008; M. Nielbock et al. 2012; S. Ragan et al. 2012; P. Sanhueza et al. 2013; J. C. Tan et al. 2013; S. Spezzano et al. 2017; A. T. Barnes et al. 2023; C. Wang & K. Wang 2023). In particular, 70 μm dark clouds represent extremely early evolutionary stages of star formation, for their young (age $<5 \times 10^4$ yr, G. Sabatini et al. 2021) cold ($T < 25$ K) and dense ($n > 10^5$ cm^{-3}) environments (e.g., P. Sanhueza et al. 2017; Y. Contreras et al. 2018; S. Feng et al. 2019; P. Sanhueza et al. 2019; E. Moser et al. 2020; E. Redaelli et al. 2021; K. Morii et al. 2024).

Recent interferometer observations, such as the Multiwavelength line-Imaging survey of the 70 μm dArk and bright clOuds (MIAO; S. Feng et al. 2020), the Atacama Large Millimeter/submillimeter Array (ALMA) Survey of 70 μm dark High-mass clumps in Early Stages (ASHES; P. Sanhueza et al. 2019), ALMA-IMF (F. Motte et al. 2022), the ALMA Three-millimeter Observations of Massive Star-forming regions (ATOMS; T. Liu et al. 2020), and the ALMA Survey of Star Formation and Evolution in Massive Protoclusters with Blue Profiles (ASSEMBLE; F. Xu et al. 2024a), have revealed that these regions are not completely quiescent with the scale below 10^4 au. Young protostellar activities, such as, fragmentation (e.g., P. Sanhueza et al. 2019; H.-L. Liu et al. 2022; X. Mai et al. 2024; K. Morii et al. 2024; F. Xu et al. 2024a; P. Sanhueza et al. 2025), infall (e.g., Y. Contreras et al. 2018; K. Morii et al. 2025), and protostellar outflows (e.g., S. Feng et al. 2016;

S. Kong et al. 2019; T. Pillai et al. 2019; S. Li et al. 2020; M. Liu et al. 2021; D. Tafoya et al. 2021; K. Kitaguchi et al. 2024) already appeared in these early star-forming regions.

Of all these initial star-forming kinematic features, the study of protostellar outflows has evolved significantly. Before the ALMA era, protostellar outflows were typically detected in more evolved stages, exhibiting a bipolar, cone-shaped structure symmetrically ejected from the protostar. Taking advantage of the high sensitivity of modern interferometers (e.g., ALMA, NOEMA), bipolar outflows have also been detected in 70 μm dark regions (e.g., S. Feng et al. 2016). Particularly, some outflows and jets exhibit curvature or asymmetry, such as "bends" and "wiggles" (e.g., N. Hirano et al. 2010; K.-S. Jhan & C.-F. Lee 2016; L. V. Ferrero et al. 2022; S. Takahashi et al. 2024), which may result from intrinsic instabilities, external interactions, or magnetic fields, though their exact origins remain uncertain (e.g., N. Hirano et al. 2010; P. Sanhueza et al. 2021; S. Takahashi et al. 2024).

In 2015, we designed the ALMA Survey of 70 μm Dark High-mass Clumps in Early Stages (ASHES; P. Sanhueza et al. 2019). At a linear resolution of $\sim$5000 au, this survey aims to investigate the physical and chemical properties of a sample of 51 70 μm dark sources, with distances ranging from 2.4 to 6.1 kpc (P. Sanhueza et al. 2019; S. Li et al. 2020; K. Morii et al. 2021a; D. Tafoya et al. 2021; S. Li et al. 2022; G. Sabatini et al. 2022; T. Sakai et al. 2022; S. Li et al. 2023; N. Izumi et al. 2024).

G034.739-00.119 (hereafter G34.74-0.12) is one of the ASHES sources, located at a kinematic distance of 5.1 ± 0.5 kpc, estimated using the Parallax-Based Distance Calculator[20] (M. J. Reid et al. 2016). The systemic velocity with respect to the local standard of rest ($V_{\rm sys,lsr}$) for G34.74-0.12 is 79.0 km s^{-1} (Y. L. Shirley et al. 2013). G34.74-0.12 has also been observed as part of the MIAO project (S. Feng et al. 2020), which investigates a sample of 26 neighboring ($\sim$1 pc), dense ($n > 10^5$ cm^{-3}), and cold (10–30 K) 70 μm dark and bright clump pairs. Both clumps of G34.74-0.12, which are at different evolutionary stages, are observed in the ASHES survey. At pc scale, IRAM-30 m observations witness a clear spatial anticorrelation between the distributions of $C^{18}O$ $J = 2$–1 and DCO^+ $J = 1$–0 in this region (S. Feng et al. 2020).

In this paper, we report young protostellar outflows, particularly one exhibiting a forked stream structure in G34.74-0.12 at a linear resolution of $\sim$5000 au. The observation and data reduction are described in Section 2. We present the observational results of the outflows and the forked stream in Section 3, discuss the possible origins of the forked stream in Section 4, and summarize our conclusions in Section 5.

2. Observation and Data Reduction

This work uses ALMA data from the ASHES project. ASHES observations toward G34.74-0.12 were carried out between 2017 November and 2018 May in Band-6 (Project ID: 2017.1.00716.S). The observations used the 12 m array (A. Wootten & A. R. Thompson 2009) for a 10-pointing mosaic, the Atacama Compact 7 m Array (ACA; S. Iguchi et al. 2009) for a three-pointing mosaic, and the total power (TP) antennas to recover the large-scale structure, with the mapping center at $18^{\rm h}55^{\rm m}09\overset{\rm s}{.}83$, $+01°33'14''.5$ (ICRS). The data set consists of a set of eight spectral windows (SPWs). Four SPWs were configured at a bandwidth of 59 MHz and a channel width of 61 kHz, corresponding to a spectral resolution of 0.17 km s^{-1}. Two SPWs were configured at a bandwidth of 59 MHz and a channel width of 31 kHz, corresponding to a spectral resolution of 0.08 km s^{-1}. Two additional broad SPWs were set at a bandwidth of 1.9 GHz and a channel width of 488 kHz, corresponding to a spectral resolution of 1.34 km s^{-1}.

Data calibration was performed using the Common Astronomy Software Application (CASA; CASA Team et al. 2022) software package versions 5.1.1 and 6.4.1. The continuum at 1.34 mm was generated from the line-free channels of the spectral windows. We use the task "uvcontsub" in CASA to perform the continuum subtraction for the spectral line data. We used *almica*[21] (H. B. Liu et al. 2015), a data combine code based on the Multichannel Image Reconstruction, Image Analysis and Display (MIRIAD) package,[22] to combine the data from the 12 m array, the ACA, and the TP in the UV domain.

The spectral line images used in this study are primary beam corrected. After mosaicking, the rms noise of each line and the dust continuum is roughly uniform across the target region, except near the edges. The line information is summarized in Table 1.

3. Result and Analysis

3.1. Protostellar Outflows and Successive Shocks

We found that the CO (2–1) emission spans a wide velocity range, from 30 km s^{-1} to 120 km s^{-1}, see channel map in Appendix A (Figure A1). To investigate the gas associated with the outflows, we integrated the velocity ranges of the blueshifted and redshifted components from 55 to 71 km s^{-1} and 85 to 92 km s^{-1}, respectively, in order to exclude emission from the dense protostellar core and foreground gas. By measuring the contribution from overlapping Galactic arms along the line of sight (M. J. Reid et al. 2009), we found that it introduces no more than a 10% uncertainty to the flux integrated over the adopted velocity range. At the signal-to-noise ratio above 8, at least four molecular outflows appeared (Figure 1, labeled I–IV), which are symmetric to the 1.3 mm dust continuum cores 1, 2, 4, and 10, respectively. Assuming a dust temperature of 15 K, these cores have masses of 9.7 $M_\odot$, 6.4 $M_\odot$, 4.1 $M_\odot$, and 3.4 $M_\odot$ (K. Morii et al. 2023). Taking into account the uncertainties in flux (10%), temperature (20%), and distance (10%), the estimated core masses have a total uncertainty of 50% (P. Sanhueza et al. 2017, 2019; K. Morii et al. 2023). Of the four outflows detected in this region, outflow I is the most prominent, extending from east to west with a projected length exceeding 1.1 pc. Several bullet-like structures appeared in both blue- and redshifted lobes on the velocity field map (i.e., moment 1, Figure 2), suggesting the presence of successive shocks.

The bipolar structure of outflow I is also traced by SiO (5–4), CH_3OH (4_2–3_1), H_2CO ($3_{0,3}$–$2_{0,2}$), H_2CO ($3_{2,2}$–$2_{2,1}$), H_2CO ($3_{2,1}$–$2_{2,0}$), and HC_3N (24–23), see Figure 2. At a typical outflow temperature of 50 K (S. Feng et al. 2015, 2022), these transitions have critical densities exceeding 2.5×10^6 cm^{-3} (Table 1), indicating that these bullet-like structures are dense gas.

To characterize the kinematic structure along the outflow propagating path, we extracted the position–velocity (PV) diagrams for both outflow I and II, with a slice width of 1.″4

[20] http://bessel.vlbi-astrometry.org/node/378

[21] https://github.com/baobabyoo/almica

[22] https://www.astro.umd.edu/~teuben/miriad/

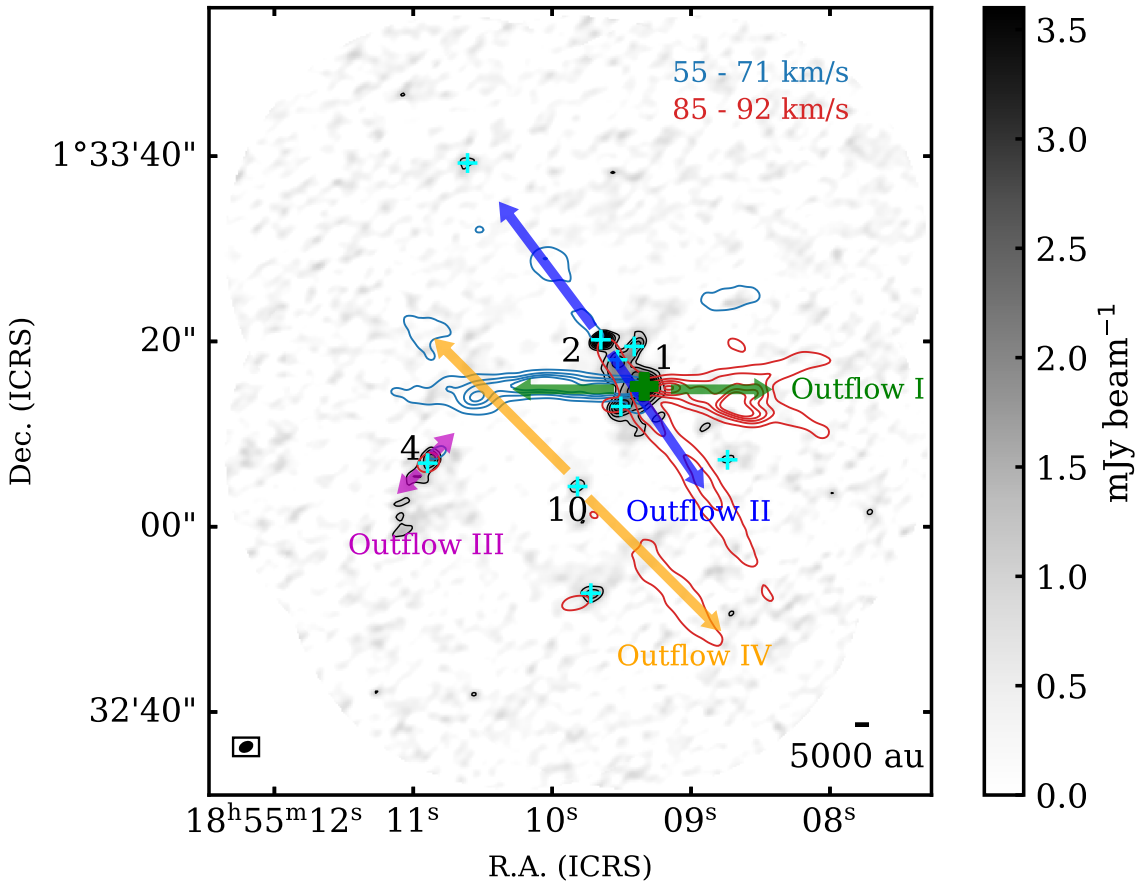

Figure 1. CO 2–1 outflow contours overlaid on 1.34 mm continuum gray map. The black contours show the emission of the continuum with levels starting from 3σ and increasing in steps of 2σ ($1\sigma = 0.3$ mJy beam^{-1} km s^{-1}). The blue and red contours represent the blue- and redshifted components, respectively. The integrated velocity ranges of the blue- and redshifted components are shown in the upper right corner ($V_{\rm sys,lsr}$ is 79.0 km s^{-1}). The contour levels for the blueshifted component start at 8σ, while those for the redshifted component start at 24σ, both increasing in increments of 16σ ($1\sigma = 0.05$ Jy beam^{-1} km s^{-1}). The green, blue, orange, and magenta bipolar arrows indicate the directions of the outflows, with the outflow IDs labeled. The green and cyan crosses indicate the positions of the identified cores, with the green cross representing the location of the most massive core 1 (9.7 $M_{\odot}$). Core IDs labeled are taken from K. Morii et al. (2023). The synthesized beam is given in the bottom left.

Table 1
Summary of the Spectral Lines

Specie	Transition	Rest Frequency[a] (GHz)	E_u/k[a] (K)	$S_{ij}\mu^2$[a] (D^2)	$n_{\rm crit}$[b] (20 K) (10^5 cm^{-3})	$n_{\rm crit}$[b] (50 K) (10^5 cm^{-3})	Velocity Resolution (km s^{-1})	rms[c] (mJy beam^{-1})	Beam Size ($''\times''$)
SiO	$J = 5$–4	217.105	31.26	47.99	9.84	8.03	0.17	9.5	1.69 × 1.25
H_2CO	$J_{K_a,K_c} = 3_{0,3}$-$2_{0,2}$	218.222	20.96	16.31	7.78	5.68	1.34	3.5	1.68 × 1.24
HC_3N	$J = 24$–23	218.325	130.98	334.19	8.35	6.89	1.34	3.5	1.69 × 1.24
CH_3OH	$J_K = 4_2$–3_1	218.440	45.46	13.91	2.16	1.09	1.34	3.5	1.68 × 1.23
H_2CO	$J_{K_a,K_c} = 3_{2,2}$–$2_{2,1}$	218.476	68.09	9.06	7.78	5.68	1.34	3.5	1.68 × 1.24
H_2CO	$J_{K_a,K_c} = 3_{2,1}$–$2_{2,0}$	218.760	68.11	9.06	7.78	5.68	1.34	3.5	1.68 × 1.24
$C^{18}O$	$J = 2$–1	219.560	15.81	0.02	0.04	0.03	1.34	3.5	1.68 × 1.23
CO	$J = 2$–1	230.538	16.60	0.02	0.04	0.03	1.34	3.5	1.59 × 1.78

Notes.
[a] Taken from the Cologne Database for Molecular Spectroscopy (CDMS; H. S. P. Müller et al. 2005).
[b] The critical densities were calculated under the assumption of optically thin conditions by solving the statistical equilibrium equations for a multilevel system, which include both downward collision rates ($\gamma_{\rm ul}$) and excitation rates ($\gamma_{\rm lu}$). The Einstein A coefficients (A_{ij}) and collisional rates (C_{ij}) at 20 K or 50 K are obtained from the Leiden atomic and molecular database (LAMDA; F. L. Schöier et al. 2005).
[c] Typical rms at the corresponding velocity resolution.

(i.e., the synthesized beam size), using the "pvextractor" tool.[23] The PV diagram of SiO (5–4) along outflow I, as shown in Figure 3, reveals several wedges/knots in both the blueshifted lobes (i.e., B1, B2, and B3) and redshifted lobes (i.e., R1 and R2). In both lobes, we do not observe a significant increase in observed velocity with distance from the driving

[23] http://pvextractor.readthedocs.org

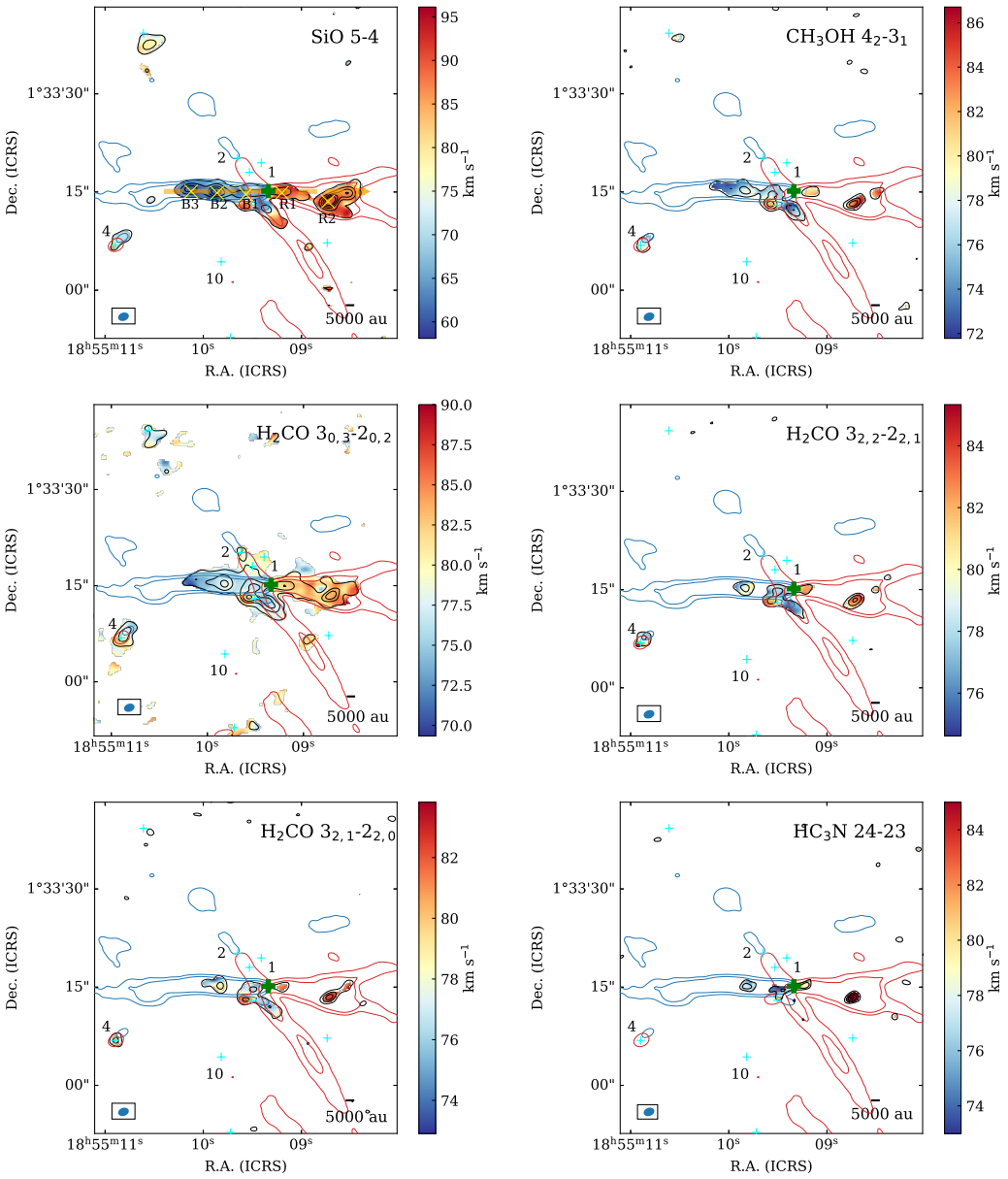

Figure 2. The intensity-weighted velocity map (moment 1) of SiO (5–4), H_2CO ($3_{0,3}$–$2_{0,2}$), H_2CO ($3_{2,2}$–$2_{2,1}$), H_2CO ($3_{2,1}$–$2_{2,0}$), CH_3OH (4_2–3_1), and HC_3N (24–23). Black contours represent their integrated intensity levels. SiO (5–4): start from 6σ and increase in steps of 16σ ($1\sigma = 0.028$ Jy beam^{-1} km s^{-1}); H_2CO ($3_{0,3}$–$2_{0,2}$): start from 6σ and increase in steps of 6σ ($1\sigma = 0.025$ Jy beam^{-1} km s^{-1}); H_2CO ($3_{2,2}$–$2_{2,1}$): start from 4σ and increase in steps of 4σ ($1\sigma = 0.020$ Jy beam^{-1} km s^{-1}); H_2CO ($3_{2,1}$–$2_{2,0}$): start from 4σ and increase in steps of 4σ ($1\sigma = 0.022$ Jy beam^{-1} km s^{-1}); CH_3OH (4_2–3_1): start from 4σ and increase in steps of 4σ ($1\sigma = 0.026$ Jy beam^{-1} km s^{-1}); HC_3N (24–23): start from 4σ and increase in steps of 1.5σ ($1\sigma = 0.024$ Jy beam^{-1} km s^{-1}). The blue and red contours represent the blue- and redshifted lobes of outflow I, II, III, and IV, respectively, as labeled in Figure 1. The green cross indicates the position of the most massive core 1, and the cyan crosses indicate the position of cores 2, 4, and 10. The orange arrow in the SiO (5–4) map represents the path for the outflow I. Yellow crosses mark the positions of knots B1, B2, B3, R1, and R2. The synthesized beam is given in the bottom left.

source (Core 1) within individual knots. This feature differs from typical "Hubble wedge" (i.e., an apparent increase in velocity with distance from the source), commonly reported in protostellar outflows (e.g., H. G. Arce & A. A. Goodman 2001; Y. Cheng et al. 2019; T. Nony et al. 2020).

Moreover, we extracted the SiO (5–4) line profiles from knot R2, knot B2, and central core 1 within a single beam area, as shown in the right panel of Figure 3. Along the E–W direction (B2-core1-R2), the SiO line profiles show broad blue- and redshifted velocity components (>20 km s^{-1}). These broad line wings, despite originating from the 70 μm dark region, are comparable in intensity to those observed in outflow regions associated with high-mass protostars (K. Qiu et al. 2007; P. Sanhueza et al. 2010; S. Feng et al. 2016; A. López-Sepulcre et al. 2016). The line profiles of all the detected lines in knots (B3-R2) are shown in Appendix D.

We note that outflow I exhibits an unanchored forked stream structure in its redshifted lobe (Figure 1). This forked stream structure is significant in the channel maps of CO (2–1) and SiO (5–4; Fork-N and Fork-S, labeled in Figures 4 and A2). Moreover, the north stream of the forked structure is also presented in CH_3OH (4_2–3_1), H_2CO ($3_{0,3}$–$2_{0,2}$), H_2CO ($3_{2,2}$–$2_{2,1}$), and H_2CO ($3_{2,1}$–$2_{2,0}$) maps (Figure 2). Both streams appear to originate from outflow I. We will discuss their origins in Section 4.3.

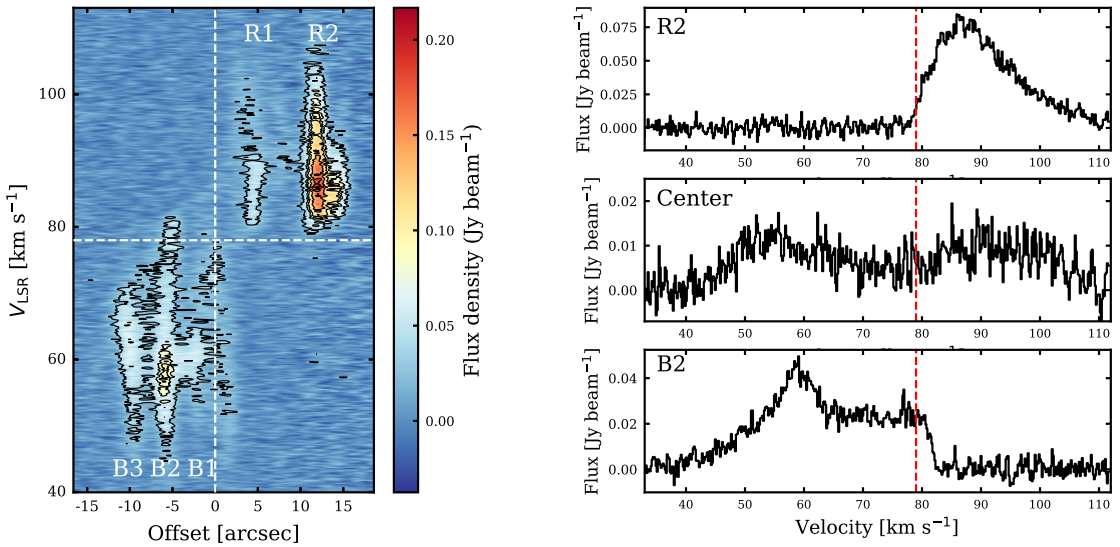

Figure 3. The left panel shows the position–velocity diagram of SiO (5–4) along the east–west direction (orange path shown in Figure 2) of outflow I with a slice width of 1.″4. The contour levels start from 8σ and increase in steps of 5σ (1σ = 0.004 Jy beam^{-1}). The vertical white dashed line indicates the position of the central protostar, and the white horizontal dashed line indicates the systemic velocity. The panel on the right shows the line profiles of SiO (5–4) extracted from a synthesized beam toward positions R2, core 1, and B2. The vertical red dashed line represents the systemic velocity (79.0 km s^{-1}) of G34.74-0.12.

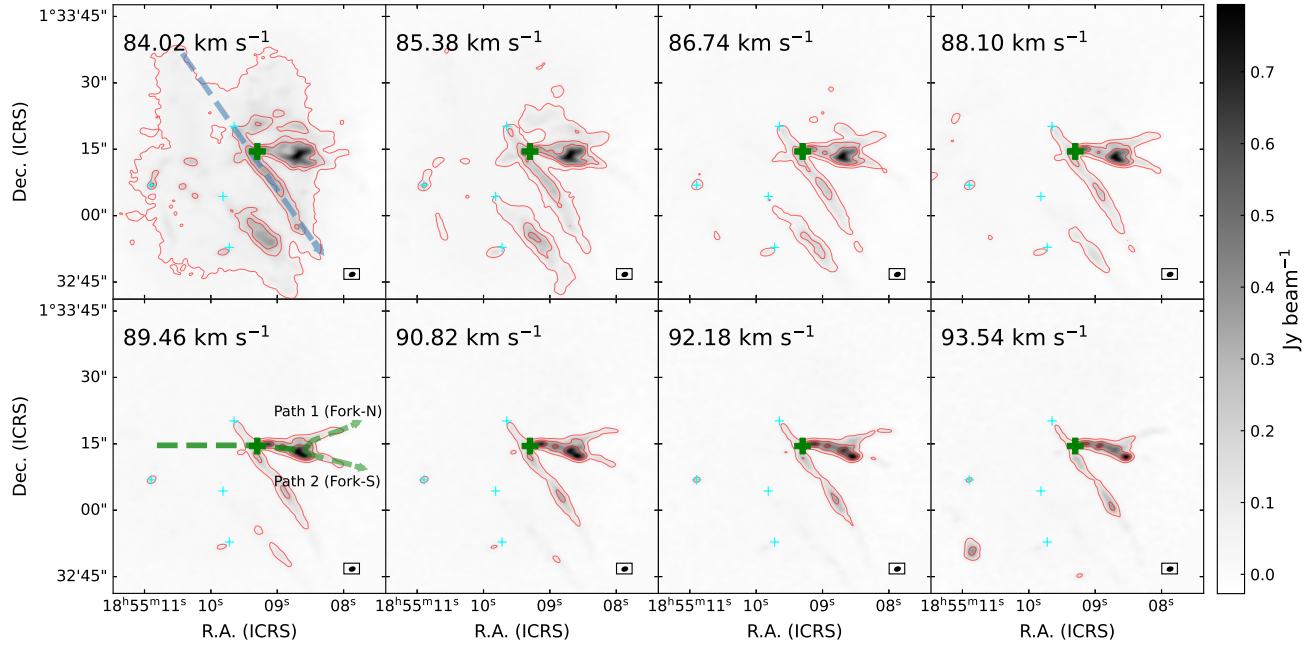

Figure 4. Channel map of the CO (2–1) displays the forked stream structure. The contour levels are 20σ, 75σ, and 110σ (1σ = 0.05 Jy beam^{-1}). The green dashed lines indicate the paths along two streams of outflow I, while the blue dashed line indicates the path of outflow II. The green cross indicates the position of core 1, and the cyan crosses indicate the position of cores 2, 4, and 10, as labeled in Figure 1. The synthesized beam is given in the bottom right.

3.2. Outflow Parameters

To characterize the physical structure of outflows, we first obtained their temperature maps by using H_2CO ($3_{0,3}$–$2_{0,2}$), H_2CO ($3_{2,2}$–$2_{2,1}$), and H_2CO ($3_{2,1}$–$2_{2,0}$) lines. These p-H_2CO transition lines serve as an effective probe for estimating the kinetic temperature of molecular gas (Y. Ao et al. 2013; X. D. Tang et al. 2017; S. Feng et al. 2019; N. Izumi et al. 2024; F. Xu et al. 2024b). We tried the rotation diagram method under the assumptions of optically thin and local thermodynamic equilibrium (LTE), as well as non-LTE approximations, to derive two kinematic temperature maps for the entire region. The non-LTE temperature map is derived using the RADEX modeling method (F. F. S. van der Tak et al. 2007). The details of the two methods are described in Appendix B. Although both methods show high agreement for the blueshifted lobes (∼55 K), the temperature derived from LTE is 20% lower than that derived from the non-LTE large velocity gradient (LVG) at the knot R2, where the forked stream structure appeared (100 K, Figure 5). Such differences are likely attributable to the assumptions of optically thin and the adopted H_2 volume density, which is also noticed at N. Izumi et al. (2024). For accuracy, we used the LVG temperature map (Figure 5) afterward.

Assuming LTE and a beam-filling factor of unity, we derived the masses, momenta, energies, and outflow rates of

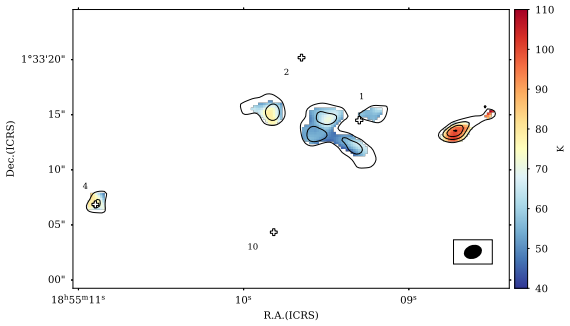

Figure 5. The temperature maps obtained from the non-LTE method using RADEX. The black contours represent the intensity of H_2CO ($3_{2,1}$–$2_{2,0}$), starting at 4σ and increasing in steps of 4σ ($1\sigma = 0.022$ Jy beam^{-1} km s^{-1}). The black cross indicates the position of the core 1, 2, 4, and 10. The synthesized beam is given in the bottom right.

the redshifted and blueshifted lobes for all the outflows from CO (2–1; listed in Table 2) using *calcu*[24] (S. Li et al. 2020). All related equations are presented in Appendix C. We adopt an excitation temperature of 64 K based on the average value from the LVG map. Given that CO emission may not trace low-density outflow components effectively, along with optical depth effects and sensitivity limitations, the derived outflow parameters may be uncertain by up to an order of magnitude (S. Li et al. 2020). Note that these parameters are not corrected for the inclination angle of outflows. Assuming a random orientation of the outflows in three-dimensional spherical space, we adopt a mean inclination angle of 57.°3, following (S. Li et al. 2020; D. Tafoya et al. 2021). The derived outflow parameters (e.g., momentum and energy) will be affected by a factor of a few (∼1.2–3.4).

Using the velocity at the full width at zero intensity (FWZI) and the projected length measured at the 8σ level (see Appendix C), the dynamical timescales for both outflow I and II are estimated to be $\sim 10^4$ yr, while those for outflow III and IV are $\sim 10^3$ yr, indicating that they are extremely young, similar to the other young protostellar outflows (e.g., S. Feng et al. 2016; M. Liu et al. 2021; A. Martínez-Henares et al. 2025). Assuming a CO abundance ratio with respect to H_2 as 10^{-4} (G. A. Blake et al. 1987), the total outflow masses of the double-sided lobes defined by $M_{\rm lobe} = M_{\rm red} + M_{\rm blue}$, are estimated to be ~ 0.8–$1.0\ M_\odot$ for the outflow I and 0.1–0.4 $M_\odot$ for the outflow II. Although Outflows I and II spatially overlap near Core 1, the overlapping region consists of the blueshifted component of Outflow I and the redshifted component of Outflow II (see Figure 1). Since the fluxes are integrated over distinct velocity ranges for each outflow, there is no overlap in velocity space. Therefore, the mass associated with each individual outflow lobe can be clearly distinguished and calculated independently. Compared to the median outflow mass (0.02 $M_\odot$) and median energy (2.1×10^{43} erg) reported in the ASHES pilot survey (S. Li et al. 2020), outflows I, II, and IV in our study appear to be more massive and energetic than the majority of outflows previously identified, indicating relatively strong star-forming activity in this region. In contrast, outflow III falls below the median in both mass and energy. This discrepancy likely results from our higher derived temperature (∼64 K, Figure 5) relative to their 15 K assumption, as well as differences in integrated flux and central core mass. However, our estimated outflow masses and energies are several orders of magnitude lower than those reported in other studies toward more evolved regions (e.g., D.-J. Liu et al. 2021; K. Yang et al. 2024).

We derive the mass loss rate of the wind ($\dot{M}_{\rm w}$) from $F_{\rm out}/v_w$, where $F_{\rm out}$ represents the mechanical force, and v_w is the wind velocity. Protostellar winds launched from accretion disks are thought to drive the outflows (R. E. Pudritz & C. A. Norman 1986; J. Bally 2016). Here we adopt a typical wind velocity of 500 km s^{-1} (H. J. G. L. M. Lamers et al. 1995; S. Li et al. 2020; A. L. Rosen 2022). Subsequently, we measure the mass accretion rates ($\dot{M}_{\rm acc}$) as $\dot{M}_{\rm acc} = k\dot{M}_{\rm w}$, where k is the ratio between the $\dot{M}_{\rm acc}$ and $\dot{M}_{\rm w}$. Theoretical models suggest that jets typically carry away approximately 30% of the infalling material (K. Tomisaka 1998; M. N. Machida & T. Matsumoto 2012; J. C. Tan et al. 2014), with the remaining mass accreting onto the protostar, corresponding to a mass accretion to mass ejection ratio of $\sim$ 3. Therefore, we adopt $k = 3$ in our analysis. We derived that the $\dot{M}_{\rm acc}$ in G34.74-0.12 is on the order of $10^{-6} M_\odot$ yr^{-1}, which is approximately equal to the maximum value found in the ASHES pilot sample, where values range from $10^{-9} M_\odot$ yr^{-1} to $10^{-6} M_\odot$ yr^{-1} (S. Li et al. 2020). These values are several orders of magnitude lower than those found in more evolved high-mass star-forming regions, where typical mass accretion rates are on the order of 10^{-5}–$10^{-3}\ M_\odot$ yr^{-1} (e.g., T. Liu et al. 2017; X. Lu et al. 2018; F.-W. Xu et al. 2023), indicating that the ongoing accretion activity in G34.74-0.12 is relatively weak compared to that in more evolved regions. The accretion rates in G34.74-0.12 suggest central stellar masses of $\sim 1\ M_\odot$ (J. Muzerolle et al. 2003; M. R. Krumholz et al. 2014).

4. Discussion

4.1. Molecular Abundances in the Outflow Regions

For the species SiO, CH_3OH, H_2CO, and HC_3N detected in the outflow region, all exhibit enhanced intensities in the outflow knots compared with the central protostar, particularly at knot R2. Assuming LTE, optically thin, and a beam-filling factor of unity, we use Equation (C1) to measure the column densities of these species (SiO, CH_3OH, H_2CO, and HC_3N) and CO at different knots. The excitation temperature is adopted uniformly for all molecules and is calculated from the average kinetic temperature derived from LVG analysis across the different knots. We derive the relative abundances with respect to CO ($N_{\rm mol}/N_{\rm CO}$) of these species for these species at knots B3, B2, B1, R1, and R2, spanning from the blueshifted lobe to the redshifted lobe of outflow I (Figure 6). Within the velocity range from $V_{\rm sys,lsr}$-2 to $V_{\rm sys,lsr}$+2 km s^{-1}, the gas emission arises from a combination of both the protostar and its associated outflow. To have the outflow-dominated component and derive the corresponding molecular abundances, we integrated the emission in the velocity range of [$V_{\rm sys,lsr}$-19,$V_{\rm sys,lsr}$-4] km s^{-1} as the blueshifted lobe, and [$V_{\rm sys,lsr}$+3,$V_{\rm sys,lsr}$+21] km s^{-1} as the redshifted lobe, based on detection thresholds of 1σ for H_2CO ($3_{0,3}$–$2_{0,2}$), CH_3OH (4_2–3_1), and HC_3N (24–23), and 2σ for SiO (5–4) and CO (2–1). The relative abundance uncertainties are mainly attributed to the temperature uncertainty derived from RADEX LVG modeling and an estimated 10% uncertainty in flux calibration.

CH_3OH shows the highest abundance with respect to CO in the entire region, followed by H_2CO, SiO, and HC_3N (Figure 6). We find that these abundances are roughly

[24] https://github.com/ShanghuoLi/calcu/tree/main

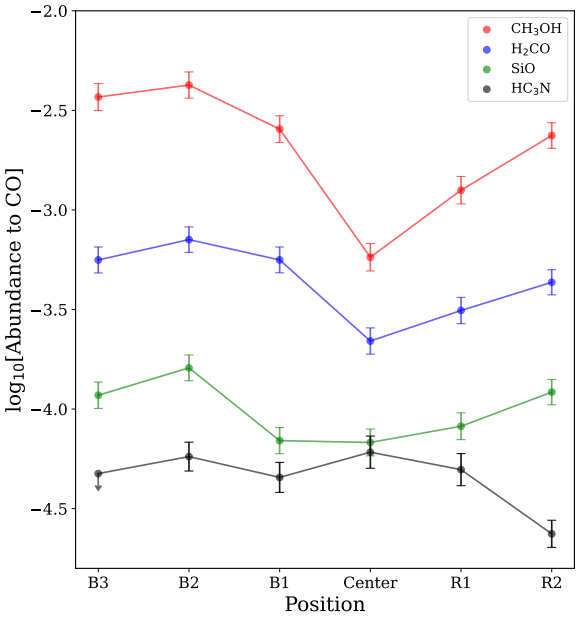

Figure 6. Molecular abundance relative to CO toward six different positions along the outflow I. The uncertainties in the relative abundance estimate arise from the temperature uncertainty derived from RADEX LVG modeling and a 10% uncertainty in the flux calibration. The downward arrow indicates the upper limit.

consistent with those observed in other young outflow regions (e.g., S. Feng et al. 2015; A. E. Higuchi et al. 2015; A. M. Burkhardt et al. 2016; S. Li et al. 2020). Except for HC_3N, all other species show similar distributions along the distance from central core 1 to the outer regions, with abundance enhancements observed in both blue- and redshifted knots compared to the central position. On the redshifted side, their enrichment pattern differs from that on the blueshifted side. In particular, at the second knot (R2), where outflow I begins to exhibit a forked stream structure, the relative abundances of H_2CO, CH_3OH, and SiO are largely enhanced compared to the center, although HC_3N exhibits a slightly decreasing trend.

4.2. The Forked Stream Structure

To investigate the velocity distribution of two outflow streams, we extracted the PV diagrams along two curve paths 1 and 2 (green dashed guideline in Figure 4). Figure 7 shows that from the point where the forked stream appears (R2) to the ends of the forked streams, the velocities exhibit a similar distribution, indicating that both outflow streams have the same origin. For comparison, we also present the PV diagram of the outflow II in Figure 7, which was extracted from the path along the outflow direction (blue dashed guideline in Figure 4). Similar to outflow I (Section 3.1), outflow II also exhibits bullet/knot structures, particularly in its redshifted lobe. In contrast to outflow I, which does not show a "Hubble wedge" structure, outflow II exhibits at least three obvious "Hubble wedge" structures (gray dashed guideline in Figure 7(c)) in the redshifted component. This structure is similar to those found in previous studies (N. Hirano et al. 2006; M. Audard et al. 2014; K. Morii et al. 2021b; S. Dutta et al. 2024; E. Guzmán Ccolque et al. 2024) and may be associated with episodic shocks.

As the CO (2–1) line is optically thick (see self-absorption features in the line profiles in Appendix D) and we cannot confirm whether the outflow is precessing, we adopt a simplified approach by connecting the central protostar directly to the symmetric outflow splitting point (marked by a blue solid triangle). This axis divides the forked structure into two streams (Figure 8(a)). We also extract five PV diagrams perpendicular to this axis toward the forked stream structure (Figures 8(b)–(f)). Although the PV diagrams reveal that the southern stream exhibits higher velocities than the northern stream along path c, both streams generally show similar velocity distributions, indicating that they originate from the same outflow.

4.3. Possible Origins of the Forked Stream Structure

The forked stream structure found in G34.74-0.12 differs from the X-shape structures commonly observed as cavity walls of outflows from both low/intermediate-mass stars (e.g., R. Bachiller et al. 2001; S. Feng et al. 2020; S. Ohashi et al. 2022; S. Dutta et al. 2024; C.-F. Liu et al. 2025) and high-mass stars (e.g., X. Chen et al. 2017; R. Fedriani et al. 2020; X. Pan et al. 2024). A precessing jet, whose direction gradually alters over time (e.g., S. Hirano & M. N. Machida 2019; S. Paron et al. 2022), as well as misaligned outflows from a binary system (e.g., C. Hara et al. 2021), can also produce an X-shape structure. However, these mechanisms cannot fully explain the observed unanchored forked stream structure in G34.74-0.12, as the forked point, located 10″ (∼0.25 pc) away from the launching center.

The northern and southern streams are found to have masses of 0.12 $M_\odot$ and 0.14 $M_\odot$, respectively (Table 2). Both streams carry comparable energy, with values of 3.99 and 5.15 $M_\odot$ km^2 s^{-2}, respectively. To examine whether a dust core along the outflow projection is responsible for the observed forked structure, we checked the 1.3 mm dust continuum emission at the corresponding location, but could not find $>3\sigma$ detection. This may be due to sensitivity limitations, with a mass surface density sensitivity of 0.32 g cm^{-2} at 3.5σ derived by (K. Morii et al. 2023), or a low-density core that is resolved out by interferometers.

One possibility is that the two streams of the forked structure result from a collision with the surrounding gas structure as the outflow propagates. This structure appears in the velocity range of 85–98 km s^{-1} in the CO 2–1 channel map (Appendix A). At the 8σ level, we notice that a filamentary structure with a width of ∼0.05 pc extends from southeast to northwest, spatially coincident with the northern stream of the forked structure along the line of sight. Therefore, the northern stream may result from a collision between the filament and the outflow. However, this structure only detected with a peak intensity of $\sim 8\sigma$ in the image of CO (2–1), which traces low critical density gas, but is not significant ($<3\sigma$) in the images of SiO (5–4), H_2CO ($3_{0,3}$–$2_{0,2}$), H_2CO ($3_{2,2}$–$2_{2,1}$), H_2CO ($3_{2,1}$–$2_{2,0}$), CH_3OH (4_2–3_1), and HC_3N (24–23), which all trace gas at higher critical densities, regardless of whether in the 12 m only or 12 m + 7 m + TP combined images.

According to the PV diagram (Figure 7), there is no significant velocity difference from the central protostar to R2, which excludes the possibility that a later, faster shock has collided with a former, slower one. Given the sudden increase in gas temperature and molecular line intensities from R1 to R2 along the outflow, it is more likely that these features result

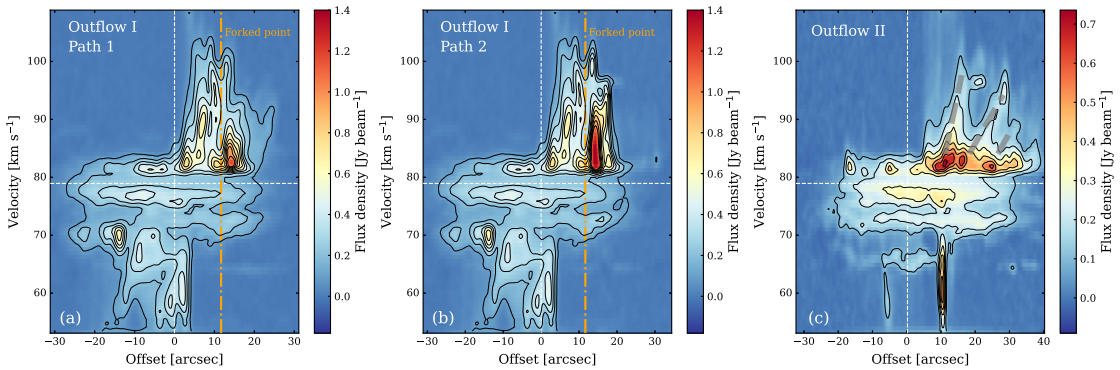

Figure 7. PV diagrams of outflow I and II extracted from the green and blue paths given in Figure 4, respectively, with a slice width of 1.″4. The colormap and the black contours are extracted from the CO (2–1) line. All contour levels start at 20σ, in steps of 20σ ($1\sigma = 0.05$ Jy beam^{-1}). The vertical white dashed line represents the position of the central protostar, the white horizontal dashed line indicates the systemic velocity, and the orange vertical dashed line marks the position where the fork-shaped structure begins to appear. The gray dashed lines shown in panel (c) indicate the "Hubble wedge" structure.

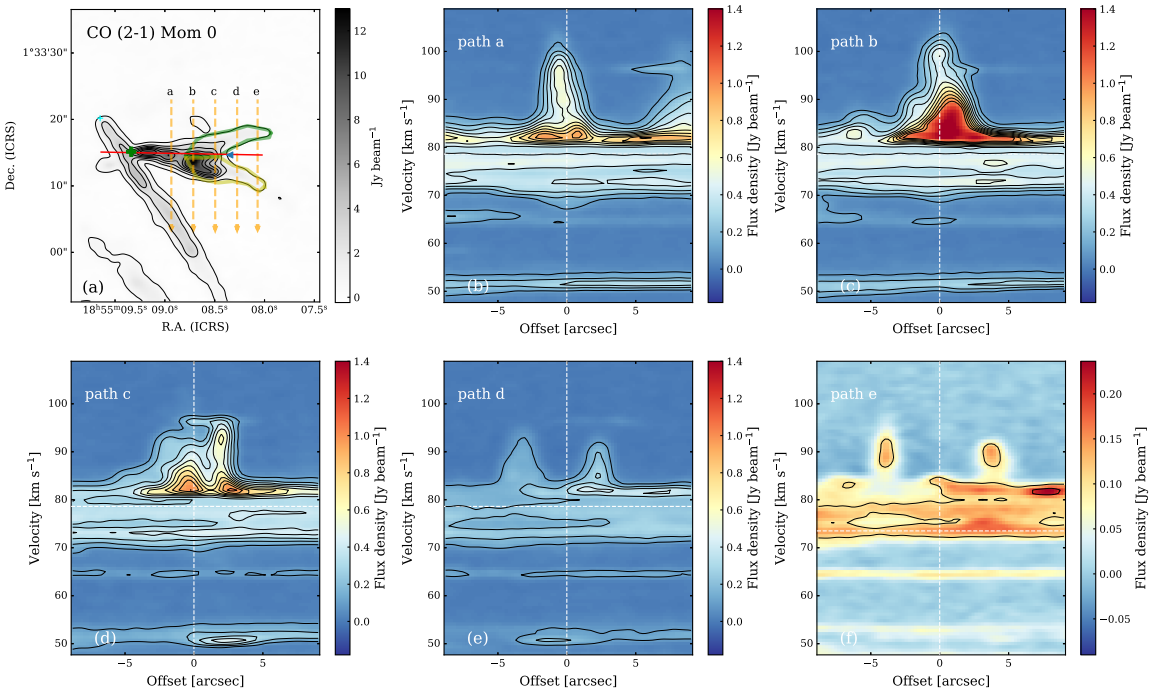

Figure 8. (a) Zoom-in on the forked stream structure in the CO (2–1) integrated intensity map. The blue triangle marks the point where the outflow splits. The red solid line connects the central protostar (green cross) to the splitting point (blue triangle). The green and yellow regions represent the northern and southern parts of the forked structure, respectively. The orange arrows indicate the five paths perpendicular to the forked structure of outflow I. (b–f) PV diagrams extracted from five different paths shown in panel (a), with a slice width of 1.″4. The colormap and the black contours are extracted from the CO (2–1) line. The vertical white dashed line represents the center of the path, and the white horizontal dashed line indicates the systemic velocity. The contour levels start at 0.1 Jy beam^{-1}, with increments of 0.1 Jy beam^{-1}.

from a collision between the outflow and a nearby dense gas structure, rather than from shock processing alone.

Therefore, the redshifted lobe of outflow I is likely interacting with either the surrounding dense gas or the nearby thin filamentary structure. When the high-velocity outflow propagates and encounters a high-density gas structure, it can form a cone-shaped structure surrounding the cloud. In projection, the two sides of this cone may appear as forked stream structures along the line of sight. Such forked structures have been predicted in the simulation of jet-cloud collisions (e.g., E. M. de Gouveia Dal Pino 1999; P. Hartigan et al. 2009). This scenario is similar to the deflected jet seen in HH 110/HH 270, which has been proposed to be the result of the collision between a jet and a nearby dense cloud (B. Reipurth et al. 1996). Observational studies have provided further evidence of interactions between outflows and their surrounding molecular core (J. A. López-Vázquez et al. 2025), as well as interactions between the outflows (L. A. Zapata et al. 2018; I. Toledano-Juárez et al. 2023). However, direct evidence of collisions between outflows and clouds remains rare, especially in cases exhibiting distinct forklike structures.

Another possible explanation is the influence of ambient pressure gradients. The pressure-confinement model (W. A. Baan & T. An 2025) suggests that ambient pressure gradients play a crucial role in shaping outflow morphologies. When the ambient pressure remains constant, outflows maintain their collimated structure, as observed in outflows II, III, IV, and the blueshifted lobe of outflow I, which exhibit

no signs of expansion. However, in regions where the ambient pressure decreases with distance, the outflow expands to maintain the pressure equilibrium with its surroundings. The redshifted lobe of outflow I appears to have initially undergone supersonic expansion near the source (core 1) before entering a region of nearly constant pressure, where it evolved into a parallel flow. At the outer edge of the cloud, the outflow encountered a sharp pressure drop at knot R2, triggering renewed expansion and widening, accompanied by significant energy dissipation. The pressure balance between outflow and the ambient medium likely resulted in the forked morphology, with the two sides of the fork marking the boundary layers of the flow. This process highlights the crucial role of ambient conditions in shaping outflow dynamics.

5. Conclusions

In the context of the ASHES project, we used ALMA observations with a linear resolution of $\sim$ 5000 au to investigate the 70 μm dark clump G34.74-0.12 at 1.3 mm, covering a 1 pc $\times$ 1 pc region. Our main conclusions are summarized as follows: (1) At least four outflows are detected by CO (2–1) in this young protostellar clump, which are spatially coincident with the dust continuum core with masses ranging from 3.4 to 9.7 $M_{\odot}$. These outflows have dynamic timescales of 10^3–10^4 yr, indicating that they are extremely young. The two most intense outflows, I and II, have momenta of 13 and 5 $M_{\odot}$ km s^{-1}, energies of 107 and 46 $M_{\odot}$ km^2 s^{-1}, respectively. (2) Along the direction of the most intensive outflow (outflow I), from the protostellar center to the shocked knots, the relative abundances of SiO, H_2CO, and CH_3OH with respect to CO generally exhibit an increasing trend. (3) Outflow I exhibits a fork-shaped structure in its redshifted lobe, with momenta of 8 and 5 $M_{\odot}$ km s^{-1} and kinetic energies of 74 and 33 $M_{\odot}$ km^2 s^{-1} in the two streams. At the forked point (knot R2), both molecular emissions and temperature are enhanced. This structure could be the result of jet/outflow-cloud interaction or pressure gradient.

Acknowledgments

We thank the anonymous referee for helpful comments. This paper makes use of the ALMA data ADS/JAO. ALMA#2017.1.00716.S (PI: P. Sanhueza). ALMA is a partnership of ESO (representing its member states), NSF (USA), and NINS (Japan), together with NRC (Canada), Molonglo Observatory Synthesis Telescope and ASIAA (Taiwan), and KASI (Republic of Korea), in cooperation with the Republic of Chile. The Joint ALMA Observatory is operated by ESO, AUI/NRAO, and NAOJ. S.L. and S.F. acknowledge support from the National Key R&D program of China grant (2025YFE0108200), National Science Foundation of China (12373023, 1213308), the starting grant at Xiamen University, and the presidential excellence fund at Xiamen University. P.S. was partially supported by a Grant-in-Aid for Scientific Research (KAKENHI Number JP22H01271 and JP23H01221) of JSPS. G.S. acknowledges the project PRIN MUR 2020 MUR BEYOND-2p (Prot. 2020AFB3FX), the PRIN MUR 2022 FOSSILS (Chemical origins: linking the fossil composition of the Solar System with the chemistry of protoplanetary disks, Prot. 2022JC2Y93), the project ASI-Astrobiologia 2023 MIGLIORA (F83C23000800005), the INAF-GO 2023 fundings PROTO-SKA (C13C23000770005), and the INAF-Minigrant 2023 TRIESTE ("TRacing the chemIcal hEritage of our originS: from proTostars to planEts"; PI: G. Sabatini).

Facility: ALMA.

Software: CASA (J. P. McMullin et al. 2007), APLpy (T. Robitaille & E. Bressert 2012; T. Robitaille 2019), Astropy (http://www.astropy.org, Astropy Collaboration et al. 2013), Matplotlib (J. D. Hunter 2007).

Author Contribution

S.L. was responsible for the data reduction, data analysis, and manuscript writing. S.F. supervised the research and provided critical revisions to the manuscript. S.P. led the ASHES project and was responsible for the observations. All authors discussed the results and contributed to the final manuscript.

Appendix A
Channel Maps

Figures A1 and A2 show the channel maps of CO (2–1) and SiO (5–4).

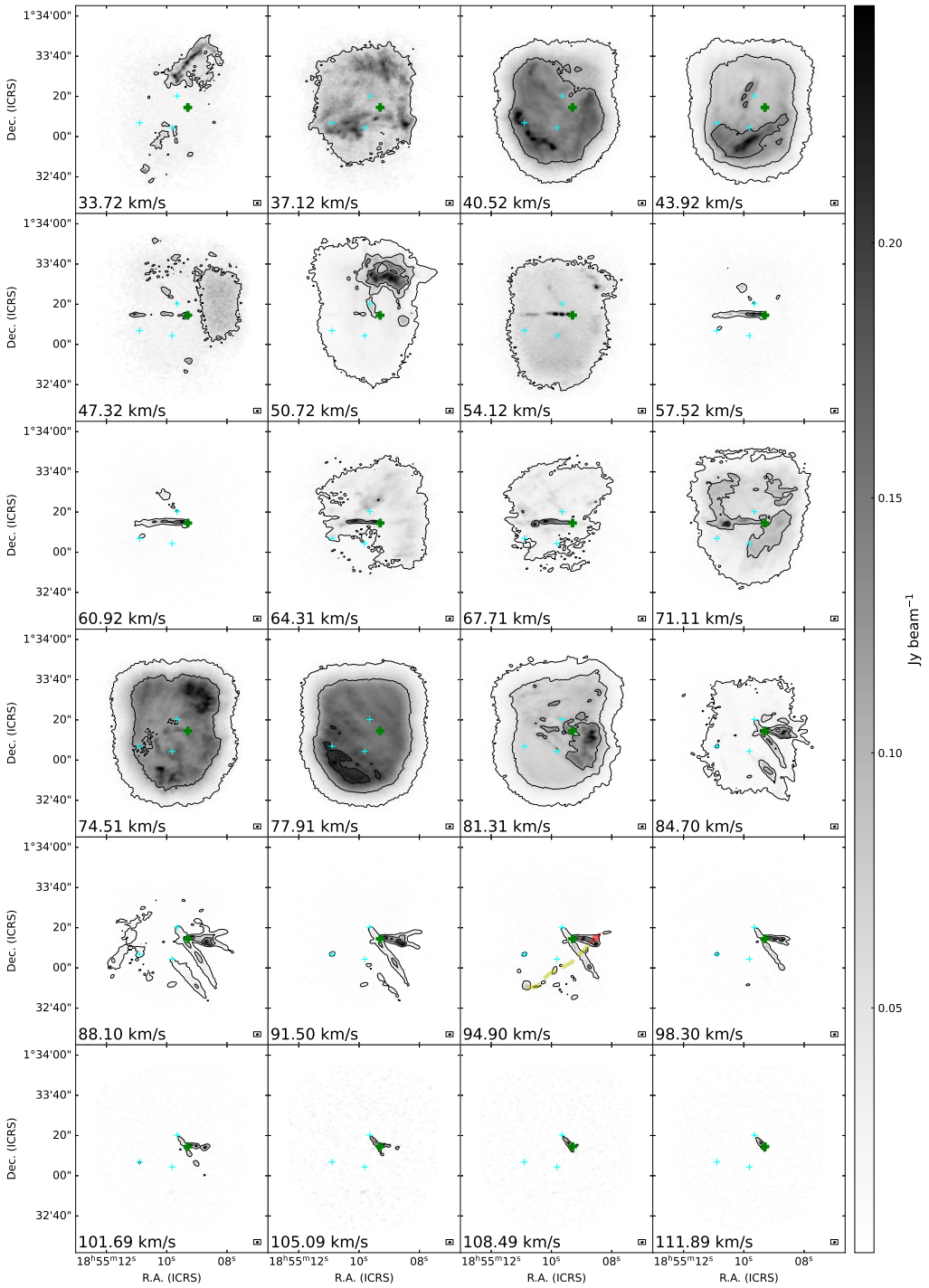

Figure A1. CO (2–1) channel map. The contour levels are 8σ, 53σ, and 113σ ($1\sigma = 0.05$ Jy beam^{-1}). The green cross indicates the position of core 1, and the cyan crosses indicate the position of cores 2, 4, and 10, as labeled in Figure 1. The yellow dashed line indicates the thin filament that may be colliding with outflow I. The red arrow highlights the site where a collision is likely occurring. The synthesized beam is given in the bottom right.

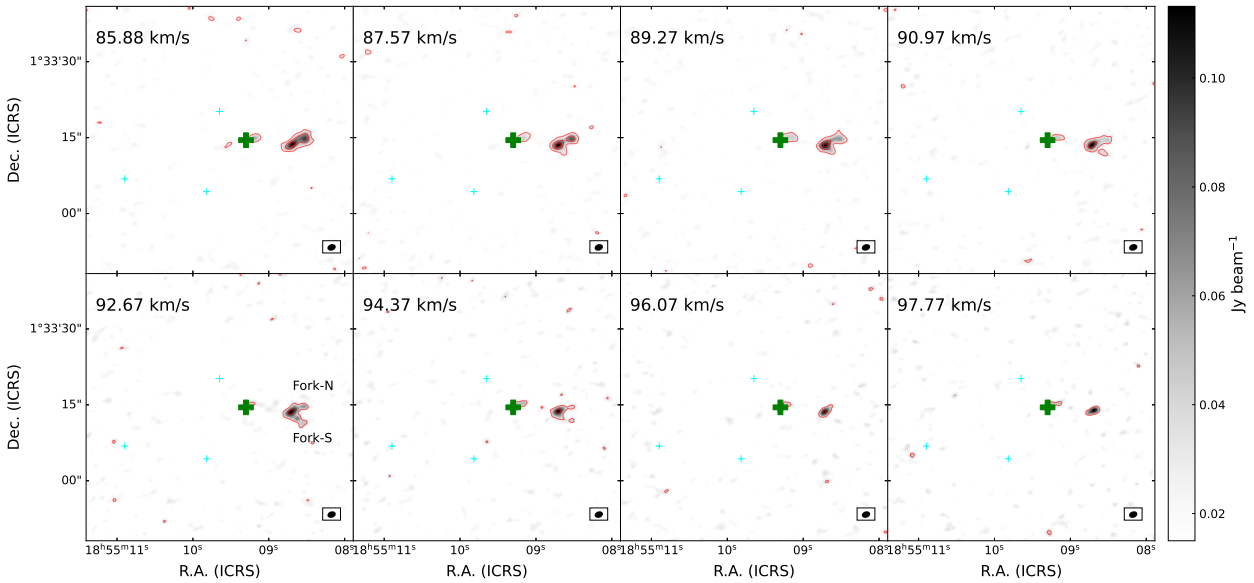

Figure A2. SiO (5–4) channel map. The contour levels start from 3σ and increase in steps of 6σ ($1\sigma = 0.013$ Jy beam^{-1}). The green cross indicates the position of core 1, and the cyan crosses indicate the position of cores 2, 4, and 10, as labeled in Figure 1. The synthesized beam is given in the bottom right.

Appendix B
Temperature Map

We performed both the LTE and non-LTE analysis to derive the temperature map of the shocked region, as shown in Figure 5. Assuming LTE and all three H_2CO lines are optically thin, we obtained the rotational temperature ($T_{\rm rot}$) in the outflow regions from the rotation diagram. For the non-LTE analysis, we adopted the Large Velocity Gradient (LVG) approximation (V. V. Sobolev 1957). The non-LTE statistical equilibrium radiative transfer code RADEX (F. F. S. van der Tak et al. 2007) and a related solver *myRadex*[25] were used in this work. Considering that the beam-filling factors are unity for all lines and a full width at mean half-maximum (FWHM) line width of 4 km s^{-1} in the fitting, we run grids of models and get the best-fit parameters from the MultiNest algorithm (F. Feroz & M. P. Hobson 2008). The number density of H_2 was set to 10^5 cm^{-3}. Collision rates were taken from Leiden Atomic and Molecular Database (LAMDA, F. L. Schöier et al. 2005).

Appendix C
Outflow Parameters and Equations

The column density of the molecule is calculated using the following equation:

$$N_{\rm mol} = \frac{3h}{8\pi^3 S_{ij}\mu^2 g_u} Q \frac{\exp\left(\frac{E_u}{k_{\rm B}T_{\rm ex}}\right)}{\exp\left(\frac{h\nu}{k_{\rm B}T_{\rm ex}}\right) - 1} \times \frac{W}{B_\nu(T_{\rm ex}) - B_\nu(T_{\rm CMB})}, \quad \text{(C1)}$$

where $k_{\rm B}$ is the Boltzmann constant, h is the Planck constant, Q represents the partition function, B_ν represents the Planck function, ν is the rest frequency, μ denotes the electric dipole moment, S_{ij} is the line strength, E_u is the upper state energy, g_u is the statistical weight of the upper level, W is the integrated intensity, $T_{\rm CMB}$ refers to the temperature of the cosmic background radiation (2.73 K), and $T_{\rm ex}$ is the excitation temperature.

We list the basic physical parameters for outflows in Table 2, including the outflow mass ($M_{\rm out}$), momentum ($P_{\rm out}$), energy ($E_{\rm out}$), and outflow rate ($\dot{M}_{\rm out}$). The outflow mass ($M_{\rm out}$) is calculated from:

$$M_{\rm out} = d^2 X_{\rm mol}^{-1} \overline{m}_{\rm H2} \int_\Omega N_{\rm mol}(\Omega) d\Omega, \quad \text{(C2)}$$

where the d is the source distance, Ω is the total solid angle, $X_{\rm mol}$ is the abundance ratio of the molecule with respect to H_2, $\overline{m}_{\rm H2}$ is the mean mass per H_2 molecule, and the $N_{\rm mol}$ is the column density of the molecule. The $P_{\rm out}$ and $E_{\rm out}$ can be estimated from:

$$P_{\rm out} = M_{\rm out} v \quad \text{(C3)}$$

$$E_{\rm out} = \frac{1}{2} M_{\rm out} v^2, \quad \text{(C4)}$$

The dynamical age and outflow rate can be estimated with:

$$t_{\rm dyn} = \frac{l_{\rm out}}{(v_{\rm max}(b) - v_{\rm max}(r))/2}, \quad \text{(C5)}$$

where $l_{\rm out}$ is the projected outflow physical length, $v_{\rm max}(b)$ and $v_{\rm max}(r)$ are the maximum velocities of blueshifted and redshifted emission, respectively.

The outflow rate ($\dot{M}_{\rm out}$) and mechanical force ($F_{\rm out}$) can be estimated from:

$$\dot{M}_{\rm out} = \frac{M_{\rm out}}{t_{\rm dyn}}, \quad \text{(C6)}$$

$$F_{\rm out} = P_{\rm out}/t_{\rm dyn}. \quad \text{(C7)}$$

[25] https://github.com/fjdu/myRadex

Table 2
Outflow Parameters[a]

Outflow	Line	Mass (M_{out}) ($M_\odot$)		Momentum (P_{out}) ($M_\odot$ km s^{-1})		Energy (E_{out}) ($M_\odot$ km^2 s^{-2})		Outflow rate ($\dot{M}_{out}$) ($M_\odot$ yr^{-1})	
		Blue[c]	Red[d]	Blue[c]	Red[d]	Blue[c]	Red[d]	Blue[c]	Red[d]
I	CO (2–1)	0.55	0.43	7.78	4.90	73.91	33.08	5.20×10^{-5}	4.09×10^{-5}
I	SiO (5–4)	0.39	0.45	6.50	4.58	63.76	28.21	3.68×10^{-5}	4.24×10^{-5}
Fork-N[b]	CO (2–1)	⋯	0.12	⋯	0.84	⋯	3.99	⋯	⋯
Fork-S[b]	CO (2–1)	⋯	0.14	⋯	1.06	⋯	5.15	⋯	⋯
II	CO (2–1)	0.16	0.24	2.17	3.03	21.66	24.45	1.60×10^{-5}	2.41×10^{-5}
II	SiO (5–4)	0.09	0.04	1.31	0.49	11.56	3.37	9.44×10^{-6}	4.41×10^{-6}
III	CO (2–1)	0.01	0.01	0.14	0.06	1.35	0.38	6.92×10^{-6}	4.62×10^{-6}
IV	CO (2–1)	0.09	0.06	1.30	0.46	13.04	1.93	1.29×10^{-5}	8.57×10^{-6}

Notes.
[a] The CO abundance is adopted as 10^{-4} (G. A. Blake et al. 1987), and the SiO abundance is adopted as 10^{-8} (S. Li et al. 2020). The excitation temperature is derived using the LVG method.
[b] "Fork-N" and "Fork-S" refer to the northern and southern streams of the forked structure in outflow I.
[c] Velocity range of the blueshifted component is [50, 75] km s^{-1}.
[d] Velocity range of redshifted component is [82, 100] km s^{-1}.

Appendix D
Line Profiles in the Knots

The line profiles of the detected lines in the blueshifted knots (Figures D1–D3) and redshifted knots (Figures D4, D5) are presented.

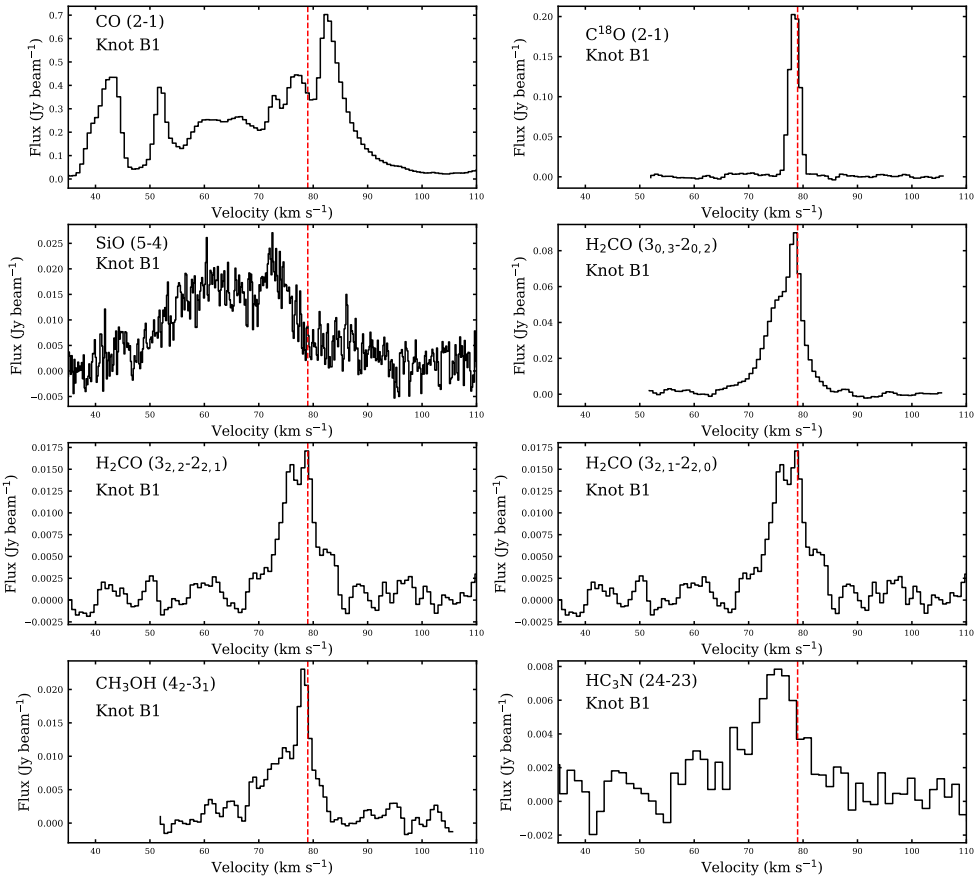

Figure D1. The line profiles extracted from a synthesized beam toward knot B1. The vertical red dashed line represents the systemic velocity (79.0 km s^{-1}) of G34.74-0.12.

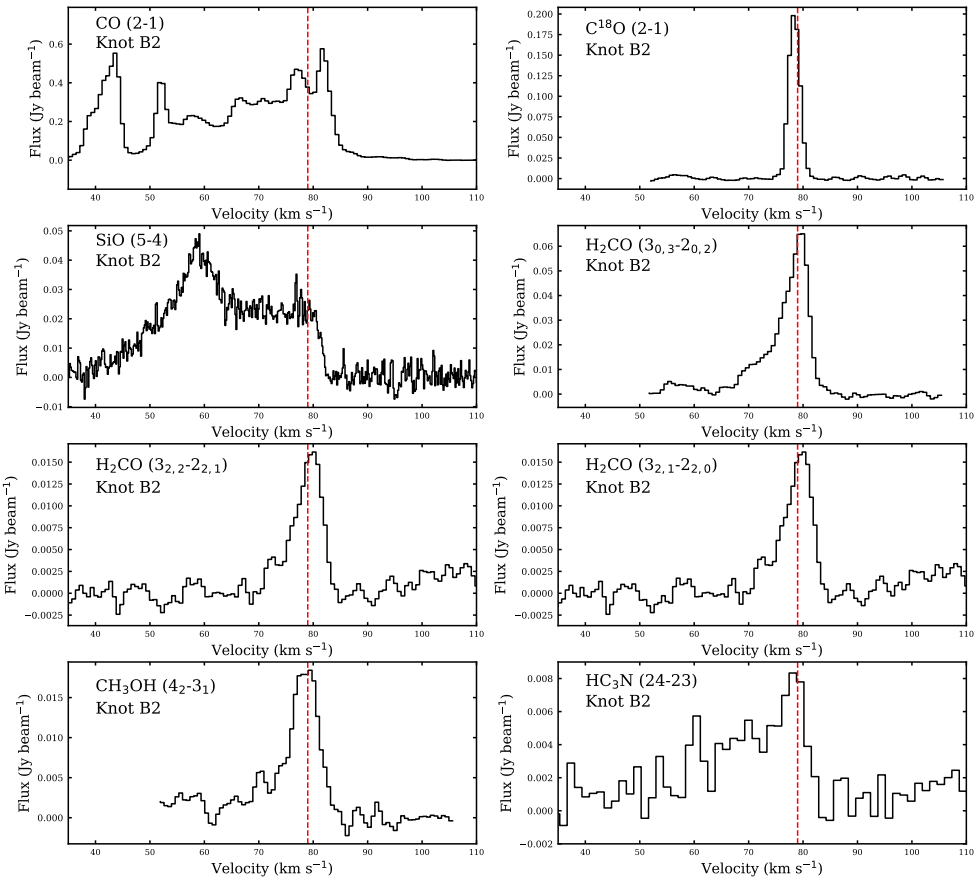

Figure D2. The line profiles extracted from a synthesized beam toward knot B2. The vertical red dashed line represents the systemic velocity (79.0 km s^{-1}) of G34.74-0.12.

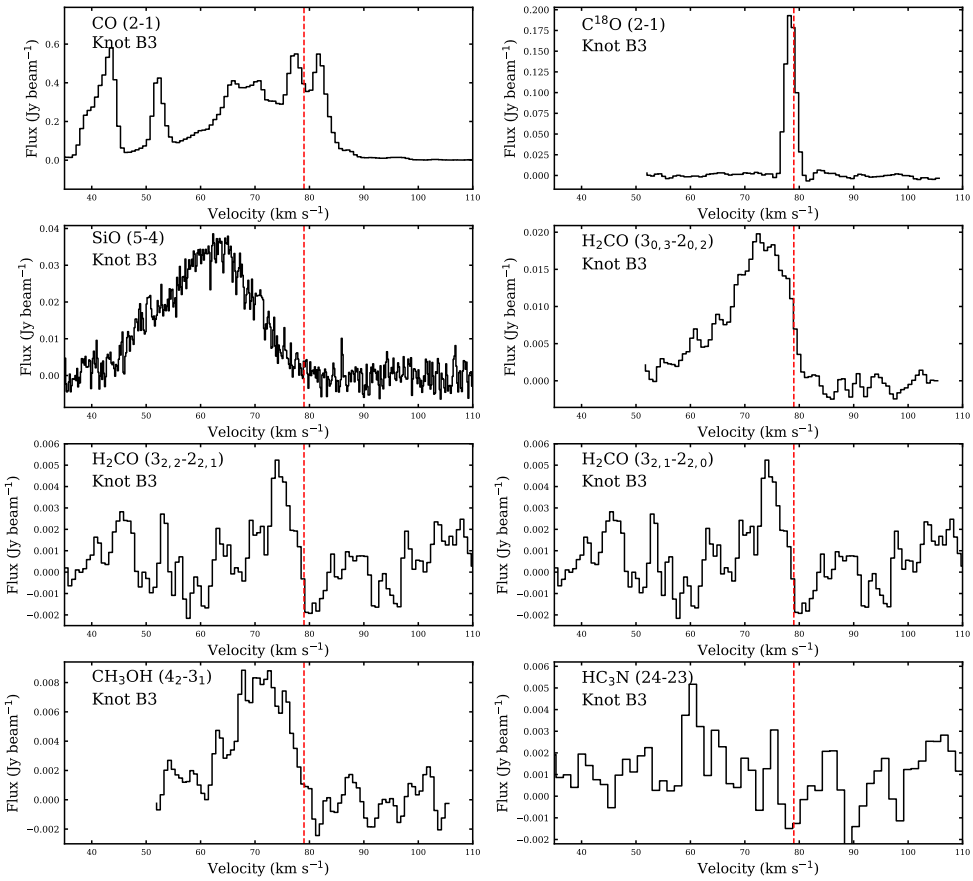

Figure D3. The line profiles extracted from a synthesized beam toward knot B3. The vertical red dashed line represents the systemic velocity (79.0 km s^{-1}) of G34.74-0.12.

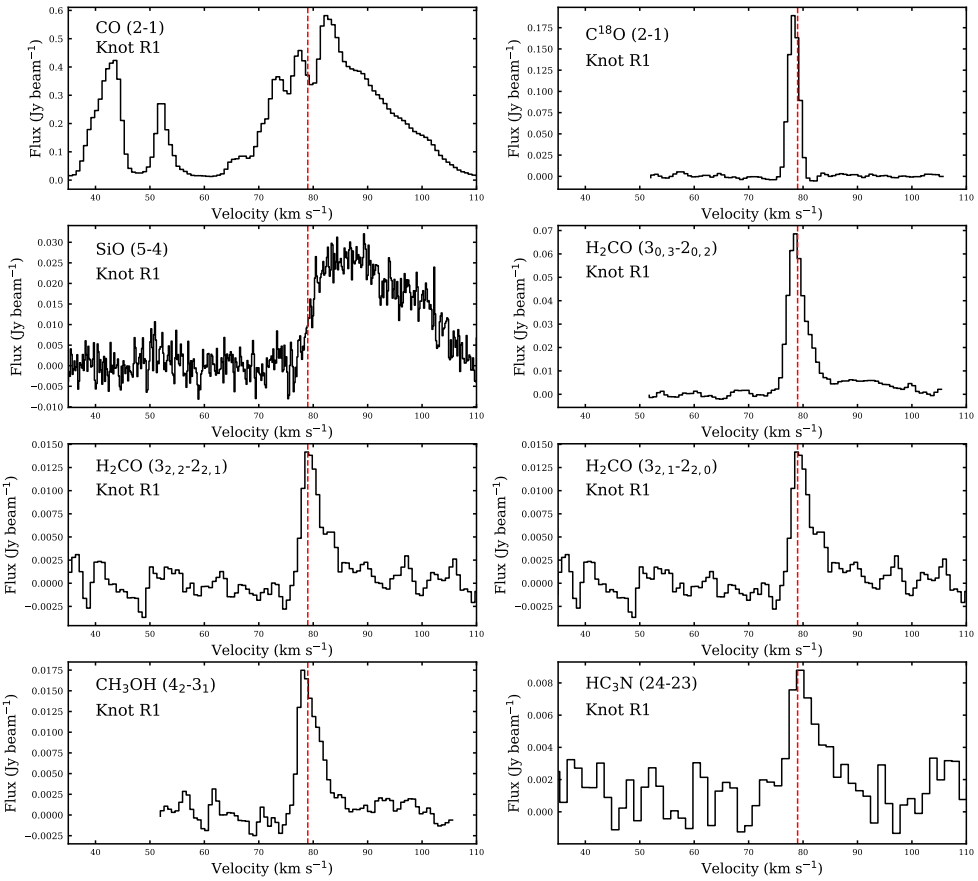

Figure D4. The line profiles extracted from a synthesized beam toward knot R1. The vertical red dashed line represents the systemic velocity (79.0 km s^{-1}) of G34.74-0.12.

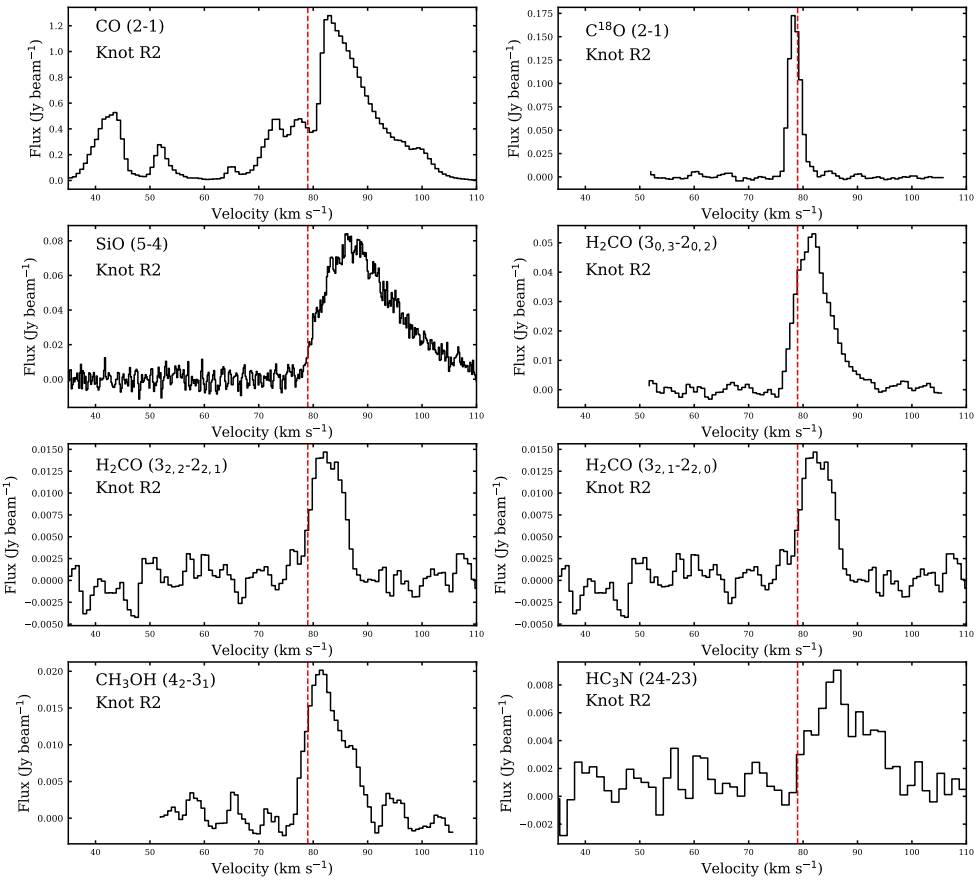

Figure D5. The line profiles extracted from a synthesized beam toward knot R2. The vertical red dashed line represents the systemic velocity (79.0 km s^{-1}) of G34.74-0.12.

ORCID iDs

Shuting Lin https://orcid.org/0000-0001-5461-1905
Siyi Feng (冯思轶) https://orcid.org/0000-0002-4707-8409
Patricio Sanhueza https://orcid.org/0000-0002-7125-7685
Ke Wang (王科) https://orcid.org/0000-0002-7237-3856
Zhi-Yu Zhang (张智昱) https://orcid.org/0000-0002-7299-2876
Yichen Zhang https://orcid.org/0000-0001-7511-0034
Fengwei Xu https://orcid.org/0000-0001-5950-1932
Junzhi Wang https://orcid.org/0000-0001-6106-1171
Kaho Morii https://orcid.org/0000-0002-6752-6061
Hauyu Baobab Liu https://orcid.org/0000-0003-2300-2626
Sheng-Yuan Liu https://orcid.org/0000-0003-4603-7119
Lile Wang https://orcid.org/0000-0002-6540-7042
Hui Li https://orcid.org/0000-0002-1253-2763
Daniel Tafoya https://orcid.org/0000-0002-2149-2660
Willem Baan https://orcid.org/0000-0003-3389-6838
Shanghuo Li https://orcid.org/0000-0003-1275-5251
Giovanni Sabatini https://orcid.org/0000-0002-6428-9806

References

Ao, Y., Henkel, C., Menten, K. M., et al. 2013, A&A, 550, A135
Arce, H. G., & Goodman, A. A. 2001, ApJL, 551, L171
Astropy Collaboration, Robitaille, T. P., Tollerud, E. J., et al. 2013, A&A, 558, A33
Audard, M., Ábrahám, P., Dunham, M. M., et al. 2014, in Protostars and Planets VI, ed. H. Beuther et al. (Tucson, AZ: Univ. Arizona Press), 387
Baan, W. A., & An, T. 2025, ApJ, 980, 119
Bachiller, R., Pérez Gutiérrez, M., Kumar, M. S. N., & Tafalla, M. 2001, A&A, 372, 899
Bally, J. 2016, ARA&A, 54, 491
Barnes, A. T., Liu, J., Zhang, Q., et al. 2023, A&A, 675, A53
Blake, G. A., Sutton, E. C., Masson, C. R., & Phillips, T. G. 1987, ApJ, 315, 621
Burkhardt, A. M., Dollhopf, N. M., Corby, J. F., et al. 2016, ApJ, 827, 21
CASA Team, Bean, B., Bhatnagar, S., et al. 2022, PASP, 134, 114501
Chen, X., Ren, Z., Zhang, Q., Shen, Z., & Qiu, K. 2017, ApJ, 835, 227
Cheng, Y., Qiu, K., Zhang, Q., et al. 2019, ApJ, 877, 112
Contreras, Y., Sanhueza, P., Jackson, J. M., et al. 2018, ApJ, 861, 14
de Gouveia Dal Pino, E. M. 1999, ApJ, 526, 862
Dunham, M. M., Crapsi, A., Evans, N. J. I., et al. 2008, ApJS, 179, 249
Dutta, S., Lee, C.-F., Johnstone, D., et al. 2024, AJ, 167, 72
Fedriani, R., Caratti o Garatti, A., Koutoulaki, M., et al. 2020, A&A, 633, A128
Feng, S., Beuther, H., Henning, T., et al. 2015, A&A, 581, A71
Feng, S., Beuther, H., Zhang, Q., et al. 2016, ApJ, 828, 100
Feng, S., Caselli, P., Wang, K., et al. 2019, ApJ, 883, 202
Feng, S., Li, D., Caselli, P., et al. 2020, ApJ, 901, 145
Feng, S., Liu, H. B., Caselli, P., et al. 2022, ApJL, 933, L35
Feroz, F., & Hobson, M. P. 2008, MNRAS, 384, 449
Ferrero, L. V., Günthardt, G., García, L., et al. 2022, A&A, 657, A110
Guzmán Ccolque, E., Fernández López, M., Vazzano, M. M., et al. 2024, A&A, 686, A143
Hara, C., Kawabe, R., Nakamura, F., et al. 2021, ApJ, 912, 34
Hartigan, P., Foster, J. M., Wilde, B. H., et al. 2009, ApJ, 705, 1073
Higuchi, A. E., Hasegawa, T., Saigo, K., Sanhueza, P., & Chibueze, J. O. 2015, ApJ, 815, 106
Hirano, N., Ho, P. P. T., Liu, S.-Y., et al. 2010, ApJ, 717, 58
Hirano, N., Liu, S.-Y., Shang, H., et al. 2006, ApJL, 636, L141
Hirano, S., & Machida, M. N. 2019, MNRAS, 485, 4667
Hunter, J. D. 2007, CSE, 9, 90
Iguchi, S., Morita, K.-I., Sugimoto, M., et al. 2009, PASJ, 61, 1
Izumi, N., Sanhueza, P., Koch, P. M., et al. 2024, ApJ, 963, 163
Jhan, K.-S., & Lee, C.-F. 2016, ApJ, 816, 32

Kitaguchi, K., Motogi, K., Fujisawa, K., Niinuma, K., & Fujiwara, R. 2024, in IAU Symp. 380, Cosmic Masers: Proper Motion Toward the Next-Generation Large Projects, ed. T. Hirota et al. (Cambridge: Cambridge Univ. Press), 227
Kong, S., Arce, H. G., Maureira, M. J., et al. 2019, ApJ, 874, 104
Krumholz, M. R., Bate, M. R., Arce, H. G., et al. 2014, in Protostars and Planets VI, ed. H. Beuther et al. (Tucson, AZ: Univ. Arizona Press), 243
Lamers, H. J. G. L. M., Snow, T. P., & Lindholm, D. M. 1995, ApJ, 455, 269
Li, S., Sanhueza, P., Lu, X., et al. 2022, ApJ, 939, 102
Li, S., Sanhueza, P., Zhang, Q., et al. 2020, ApJ, 903, 119
Li, S., Sanhueza, P., Zhang, Q., et al. 2023, ApJ, 949, 109
Liu, C.-F., Shang, H., Johnstone, D., et al. 2025, ApJ, 979, 17
Liu, D.-J., Xu, Y., Li, Y.-J., et al. 2021, ApJS, 253, 15
Liu, H. B., Galván-Madrid, R., Jiménez-Serra, I., et al. 2015, ApJ, 804, 37
Liu, H.-L., Tej, A., Liu, T., et al. 2022, MNRAS, 510, 5009
Liu, M., Tan, J. C., Marvil, J., et al. 2021, ApJ, 921, 96
Liu, T., Evans, N. J., Kim, K.-T., et al. 2020, MNRAS, 496, 2790
Liu, T., Lacy, J., Li, P. S., et al. 2017, ApJ, 849, 25
López-Sepulcre, A., Watanabe, Y., Sakai, N., et al. 2016, ApJ, 822, 85
López-Vázquez, J. A., Fernández-López, M., Girart, J. M., et al. 2025, A&A, 695, A236
Lu, X., Zhang, Q., Liu, H. B., et al. 2018, ApJ, 855, 9
Machida, M. N., & Matsumoto, T. 2012, MNRAS, 421, 588
Mai, X., Liu, T., Liu, X., et al. 2024, ApJL, 961, L35
Martínez-Henares, A., Jiménez-Serra, I., Vastel, C., et al. 2025, A&A, 699, A382
McMullin, J. P., Waters, B., Schiebel, D., Young, W., & Golap, K. 2007, in ASP Conf. Ser. 376, Astronomical Data Analysis Software and Systems XVI ed. R. A. Shaw, F. Hill, & D. J. Bell (San Francisco, CA: ASP), 127
Morii, K., Sanhueza, P., Csengeri, T., et al. 2025, ApJ, 979, 233
Morii, K., Sanhueza, P., Nakamura, F., et al. 2021a, ApJ, 923, 147
Morii, K., Sanhueza, P., Nakamura, F., et al. 2023, ApJ, 950, 148
Morii, K., Takahashi, S., & Machida, M. N. 2021b, ApJ, 910, 148
Morii, K., Sanhueza, P., Zhang, Q., et al. 2024, ApJ, 966, 171
Moser, E., Liu, M., Tan, J. C., et al. 2020, ApJ, 897, 136
Motte, F., Bontemps, S., Csengeri, T., et al. 2022, A&A, 662, A8
Müller, H. S. P., Schlöder, F., Stutzki, J., & Winnewisser, G. 2005, JMoSt, 742, 215
Muzerolle, J., Hillenbrand, L., Calvet, N., Briceño, C., & Hartmann, L. 2003, ApJ, 592, 266
Nielbock, M., Launhardt, R., Steinacker, J., et al. 2012, A&A, 547, A11
Nony, T., Motte, F., Louvet, F., et al. 2020, A&A, 636, A38
Ohashi, S., Codella, C., Sakai, N., et al. 2022, ApJ, 927, 54
Pan, X., Qiu, K., Yang, K., Cao, Y., & Zhang, X. 2024, A&A, 684, A141
Paron, S., Mast, D., Fariña, C., et al. 2022, A&A, 666, A105
Pillai, T., Kauffmann, J., Zhang, Q., et al. 2019, A&A, 622, A54
Pudritz, R. E., & Norman, C. A. 1986, ApJ, 301, 571
Qiu, K., Zhang, Q., Beuther, H., & Yang, J. 2007, ApJ, 654, 361
Ragan, S., Henning, T., Krause, O., et al. 2012, A&A, 547, A49
Rathborne, J. M., Jackson, J. M., & Simon, R. 2006, ApJ, 641, 389
Redaelli, E., Bovino, S., Giannetti, A., et al. 2021, A&A, 650, A202
Reid, M. J., Dame, T. M., Menten, K. M., & Brunthaler, A. 2016, ApJ, 823, 77
Reid, M. J., Menten, K. M., Zheng, X. W., et al. 2009, ApJ, 700, 137
Reipurth, B., Raga, A. C., & Heathcote, S. 1996, A&A, 311, 989
Robitaille, T. 2019, APLpy v2.0: The Astronomical Plotting Library in Python, Zenodo, doi:10.5281/zenodo.2567476
Robitaille, T., & Bressert, E. 2012, APLpy: Astronomical Plotting Library in Python, Astrophysics Source Code Library, ascl:1208.017
Rosen, A. L. 2022, ApJ, 941, 202
Sabatini, G., Bovino, S., Giannetti, A., et al. 2021, A&A, 652, A71
Sabatini, G., Bovino, S., Sanhueza, P., et al. 2022, ApJ, 936, 80
Sakai, T., Sanhueza, P., Furuya, K., et al. 2022, ApJ, 925, 144
Sanhueza, P., Contreras, Y., Wu, B., et al. 2019, ApJ, 886, 102
Sanhueza, P., Garay, G., Bronfman, L., et al. 2010, ApJ, 715, 18
Sanhueza, P., Girart, J. M., Padovani, M., et al. 2021, ApJL, 915, L10
Sanhueza, P., Jackson, J. M., Foster, J. B., et al. 2013, ApJ, 773, 123
Sanhueza, P., Jackson, J. M., Zhang, Q., et al. 2017, ApJ, 841, 97
Sanhueza, P., Liu, J., Morii, K., et al. 2025, ApJ, 980, 87
Schöier, F. L., van der Tak, F. F. S., van Dishoeck, E. F., & Black, J. H. 2005, A&A, 432, 369
Shirley, Y. L., Ellsworth-Bowers, T. P., Svoboda, B., et al. 2013, ApJS, 209, 2
Sobolev, V. V. 1957, SvA, 1, 678
Spezzano, S., Caselli, P., Bizzocchi, L., Giuliano, B. M., & Lattanzi, V. 2017, A&A, 606, A82
Tafoya, D., Sanhueza, P., Zhang, Q., et al. 2021, ApJ, 913, 131
Takahashi, S., Machida, M. N., Omura, M., et al. 2024, ApJ, 964, 48
Tan, J. C., Beltrán, M. T., Caselli, P., et al. 2014, in Protostars and Planets VI, ed. H. Beuther et al. (Tucson, AZ: Univ. Arizona Press), 149
Tan, J. C., Kong, S., Butler, M. J., Caselli, P., & Fontani, F. 2013, ApJ, 779, 96
Tang, X. D., Henkel, C., Menten, K. M., et al. 2017, A&A, 598, A30
Toledano-Juárez, I., de la Fuente, E., Trinidad, M. A., Tafoya, D., & Nigoche-Netro, A. 2023, MNRAS, 522, 1591
Tomisaka, K. 1998, ApJL, 502, L163
van der Tak, F. F. S., Black, J. H., Schöier, F. L., Jansen, D. J., & van Dishoeck, E. F. 2007, A&A, 468, 627
Wang, C., & Wang, K. 2023, A&A, 674, A46
Wootten, A., & Thompson, A. R. 2009, IEEEP, 97, 1463
Xu, F., Wang, K., Liu, T., et al. 2024a, ApJS, 270, 9
Xu, F., Wang, K., Liu, T., et al. 2024b, RAA, 24, 065011
Xu, F.-W., Wang, K., Liu, T., et al. 2023, MNRAS, 520, 3259
Yang, K., Qiu, K., & Pan, X. 2024, A&A, 684, A140
Zapata, L. A., Fernández-López, M., Rodríguez, L. F., et al. 2018, AJ, 156, 239